Materials Chemistry and Physics 346 (2025) 131302

Contents lists available at ScienceDirect

Materials Chemistry and Physics

journal homepage: www.elsevier.com/locate/matchemphys

Performance enhancement of Titanium–Zirconium–Hafnium–Niobium–Tantalum high-entropy alloys with copper content

Md. Ahasan [a,*], Kiran Kumar Billa [b], Gollapalli Veera Satya Srinivas [a], D.S. ChandraMouli [c], R.S. Srikanth Varma [d], P. Sri Gowri Padmaja [e], Rama Bhadri Raju Chekuri [d], Gattem Naga Lakshmi [f]

[a] Department of Mechanical Engineering, Aditya University, Surampalem, Andhra Pradesh, 533437, India
[b] Department of Mechanical Engineering, Sasi Institute of Technology and Engineering, Tadepalligudem, Andhra Pradesh, 534101, India
[c] Department of Mechanical Engineering, MallaReddy (MR) Deemed to be University, Hyderabad, Telangana, 500100, India
[d] Department of Mechanical Engineering, Sagi Rama Krishnam Raju Engineering College, Bhimavaram, Andhra Pradesh, 534204, India
[e] Department of Mechanical Engineering, Aditya University, Surampalem, Andhra Pradesh, 533437, India
[f] Department of Electrical and Electronics Engineering, Aditya University, Surampalem, Andhra Pradesh, 533437, India

HIGHLIGHTS

- Investigates Cu (0–20 %) effects on Ti–Zr-Hf-Nb-Ta high-entropy alloys.
- Cu enhances hardness, yield strength, and phase stability.
- Microstructural evolution forms Cu-rich regions and secondary phases.
- Thermal researches show improved degradation resistance with Cu addition.
- MATLAB simulations validate phase, mechanical, and thermal behavior.

ARTICLE INFO

Keywords:
High-entropy alloys
Copper content
Phase analysis
Hardness
Magnetism
Thermal stability
Yield strength
Alloy behaviour

ABSTRACT

High-entropy alloys show outstanding mechanical, thermal, and magnetic properties, primarily due to its unique atomic structure, high mixing entropy, and slow diffusion characteristics. This research analyses the variations in copper content (0–20 %) concerning the phase constitution, mechanical properties, thermal stability, and magnetism of Titanium–Zirconium–Hafnium–Niobium–Tantalum (Ti–Zr-Hf-Nb-Ta) high-entropy alloys. The alloying procedure is realized by the powder metallurgy technique, comprising powder blending, compaction, and sintering under controlled conditions. The phase analyses revealed the influence of copper to promote microstructural evolution with the setting up of copper enrichment and multiple microscopic secondary phases that altered the mechanical and magnetic property response of the alloy. Analysis revealed that with increasing copper content, both hardness and yield strength decrease, indicating a softening effect with higher copper addition, and there is also a compromise between strength and ductility. From thermal stability research, it is concluded that copper enhances the phase stability and increases degradation temperatures. Copper modified saturation magnetization and curie temperature with appreciable segregation mechanisms to modify its ferro-magnetic response. Besides, phase transformations, mechanical behaviours, and thermal responses are also simulated by MATLAB to extrapolate computational validations for alloy behaviour. The research implies that copper-modified Ti–Zr-Hf-Nb-Ta high-entropy alloys are considered an advanced structural and functional application by tuning parameters for mechanical strength, thermal stability, and magnetic behaviour for wide-spread acceptance in engineering applications.

* Corresponding author.
E-mail addresses: mdahasankhan@gmail.com (Md. Ahasan), drkiran.billa@sasi.ac.in (K.K. Billa), satyasrinivas4@gmail.com (G.V. Satya Srinivas), dkmouli1986@gmail.com (D.S. ChandraMouli), rssvarma.mech@gmail.com (R.S.S. Varma), gowripadmaja314@gmail.com (P.S. Gowri Padmaja), bhadri.mech@gmail.com (R.B. Raju Chekuri), naga3811@gmail.com (G.N. Lakshmi).

https://doi.org/10.1016/j.matchemphys.2025.131302
Received 20 March 2025; Received in revised form 6 June 2025; Accepted 13 July 2025
Available online 18 July 2025

1. Introduction

In recent times, research in alloys has shown that the incorporation of various elements into an alloy usually creates metallic compounds that have lower physical and mechanical properties [1]. This is a technique that allows for cost-effective, dynamic, and sustainable production of metallic components using advanced properties and configurations in a modern manufacturing environment [2]. As these industries strive to increase product performance, efficiency, and market competitiveness, the significance of Powder Metallurgy (PM) continues to grow [3]. Many nanocomposites of various alloys, which include Magnesium–Titanium–Silicon Carbide (Mg–Ti–SiC) nanocomposites, and Alpha-phase Alumina (α-Al_2O_3)-based alloys are produced on a commercial scale using this technique [4,5]. For this purpose, PM appears today as a viable alternative to some methods such as friction stir processing, stir casting, and thermal methods [6–8]. Recent technological developments in the alloy industry have brought about the birth of High-Entropy Alloys (HEAs) initiated by Yie and co-workers [9]. HEAs are materials innovatively prepared via mixing of five or more principal constituents, whose atomic ratio of percentage fractions ranges from 5 % to 35 % [10]. The unique composition of HEAs delivers four key features: lattice distortion, extreme orderliness of mixing entropy, cocktail effect, and slow rates of diffusion [11]. These are important reasons for better diversity in the formation of phases and lie in the great advantage of exceptional corrosion resistance, exceptional thermal oxidation resistance, and exceptional mechanical strength as compared to conventional alloys [12]. Due to the exceptional attributes of HEAs, these metals are being used as functional materials in various applications such as superconductors [13], thermoelectrics, hydrogen storage, magnetocaloric systems, and soft magnetic materials [14]. It seems that among the HEA systems, the ones having Fe, Co, Ni, Cr, and Cu are the most extensively calculated [15]. However, most of the HEAs formed are mainly Face-Centred Cubic (FCC) and have a single phase that eventually leads to lower strength and higher ductility [16]. One method through which mechanical strength is increased is by the formation of a secondary phase [17]. However, this procedure often comes at the expense of reduced ductility while increasing hardness and yield strength [18]. Several studies demonstrate that HEAs containing Copper (Cu) improve yield strength from 188.04 MPa to 350.63 MPa and hardness from 165.35 Vickers Hardness (HV) to 215.84 HV through reinforcement with a Cu-rich phase [19]. HEA/Cu alloys have also been calculated to a large extent because their oxidation resistance and mechanical properties are further elevated [20]. Md.Ahasan et al. [21] investigated through incremental loading till failure, the densification and strain hardening behavior were examined. In-depth discussions were held regarding the impact of aspect ratio and the addition of TiB_2 to aluminum on formability. Instantaneous density coefficient, work hardening exponent, instantaneous strain rate sensitivity, stress ratio parameters, and densification reached were examined. Md.Ahasan et al. [22] conducted experiments and formulated a constitutive relation between flow strain and stress at various heat (200, 300, 400, and 500 °C) and different strain rates (0.12, 0.14, 0.16, and 0.18 s^{-1}). This relation was used to predict the densification attained and the behaviour of deformation for various deformation levels and temperatures. The software DEFORM 2D, which was based on finite element analysis (FEA), was used to forecast the density distribution and the positions of the minimum and maximum density zones. The critical damage value was determined, and the damage mechanism controlling the densification process was established. Md.Ahasan et al. [23] investigated to assess closely whether the predicted response values from both RSM and NN approaches matched the experimental values by comparing them. It was discovered that the preform Final Density (FD) rises in response to load and the initial preform density of the sintered preform, and that the aspect ratio has minimal impact on densification. Using NN and RSM approaches, the FD of aluminium and titanium diboride (Al–TiB2) sintered preforms for various beginning preform and aspect ratio conditions. Zeng et al. [24] enhanced the HEA by developing a binary-phase CuNiTiNbCr twin-phase alloy film in the Cu rich FCC alloy along with an amorphous phase growth deposited at various bias voltages under high-power impulse magnetron sputtering conditions. Xia et al. [25] developed and synthesized a set of reduced activation FeCrV-based HEAs with differing Ti concentrations to analyze the phase structures, thermodynamic parameters, and nano-hardness relationship. Yue et al. [26] fabricated AlCoCrFeNi HEAs with Ti using laser cladding to increase the corrosion resistance of the coating. This examined the effect of Ti content on the microstructure of the coatings. Liu et al. [27] successfully bonded Cf/SiC to GH3536, thereby facilitating the direct formation of Fe–W–Ni–Cr–Cu HEA during brazing. The research investigated the formation process and martensitic phase transformation. Meng et al. [28] investigated quantity of cladding layers affects the composition of elements and their impact on the microstructure, phase constitution, wear resistance, electrochemical, and microhardness properties of HEA coatings. Kwon et al. [29] determined the enthalpy of mixing fluctuations in the solid-solution and amorphous phases of ten binary alloys, using the extended Miedema theory to calculate the Gibbs energy of mixing for a quinary alloy system. An et al. [30] examined the impacts of HEA particle reinforcement on 7075 Aluminium Matrix Composites' (AMCs') microstructure, mechanical characteristics, and overall performance.

1.1. Research motivation

This research is motivated by the growing interest in HEA, with exceptional properties, such as excellent corrosion resistance, strength, and thermal stability, which makes it very desirable to research these alloys. HEAs hold promise, but often present a challenge for the mechanical and physical performance in the balance of strength and ductility. Although copper (Cu) has been reported to enhance hardness and thermal stability in some HEA systems through secondary phase strengthening, its effect is highly dependent on alloy composition and remains poorly understood in refractory multi-principal element systems like Ti–Zr-Hf-Nb-Ta. The Heusler alloy improved hardness, thermal stability, and magnetic behavior by adding Cu content to HEAs; however, much remains to be known regarding the effect of altering the content of Cu on these properties. In addition, it does not know about the possible impacts of the content of Cu on thermal behavior, phase constitution, and magnetic properties, especially in Ti–Zr-Hf-Nb-Ta HEAs. These research gaps are attempted to be bridged by a systematic investigation on the effect of Cu on the mechanical properties, thermal stability, microstructure, and magnetic behavior of Ti–Zr-Hf-Nb-Ta HEAs for the optimization of their performance and adaptation for specific industrial applications.

1.2. Objectives of the research

This research examines the impacts of varying Cu percentage (0–20 %) on the phase constitution, thermal stability, mechanical properties, and magnetic behavior of Ti–Zr-Hf-Nb-Ta high-entropy alloys. The structural changes, such as Cu-rich regions and secondary phases, are analyzed to assess their impact on alloy stability. Mechanical properties such as yield strength, hardness, and strength-ductility balance also be evaluated to optimize performance. The phase stability, thermal degradation temperatures, and oxidation resistance of these phases indicate the thermal stability. Additionally, the present research discusses the influence of Cu on the magnetic characteristics, such as curie temperature saturation magnetization, and the effects of element segregation. Thus, the current research has concentrated on enhancing the knowledge on the Cu-containing HEAs by optimizing the composition and increasing their versatility in the high-performance materials use sectors for different industrial applications.

2. Materials and methods

This research adopts a structured and integrative approach, as depicted in Fig. 1, to investigate the influence of varying copper content on the phase behavior, mechanical performance, thermal stability, and magnetic properties of Ti–Zr-Hf-Nb-Ta HEAs. The methodology combines experimental synthesis and characterization with computational modeling to provide a comprehensive understanding of material behavior. The copper content is systematically varied between 0 and 20 at. % to evaluate its role in modifying the alloy system. Each stage in the experimental workflow from materials selection to final output plays a critical role in ensuring the development of an optimized, multifunctional HEA suitable for structural and magnetic applications.

❖ Materials Selection & Experimentation

This stage begins with the selection of high-purity elemental powders Ti–Zr-Hf-Nb-Ta, chosen for their ability to form stable solid solutions and contribute to high-temperature and mechanical strength. Cu is introduced as a doping element to modify phase stability and magnetic behavior. The Cu content is varied incrementally (0 %, 5 %, 10 %, 15 %, and 20 %). Initial testing includes basic physical and chemical characterization to establish a performance baseline before alloy formation.

❖ **Phase Constitution Analysis and Modelling**

In this phase, phase formation tendencies and stability of different Cu-doped compositions are analyzed using both experimental (e.g., XRD) and computational (e.g., Thermo-Calc or CALPHAD) tools. The aim is to detect phase separation, secondary phase formation, and copper-rich zones. This modeling helps predict the likelihood of solid solution versus intermetallic formation under equilibrium and non-equilibrium conditions.

❖ **Material Formation & Experimentation**

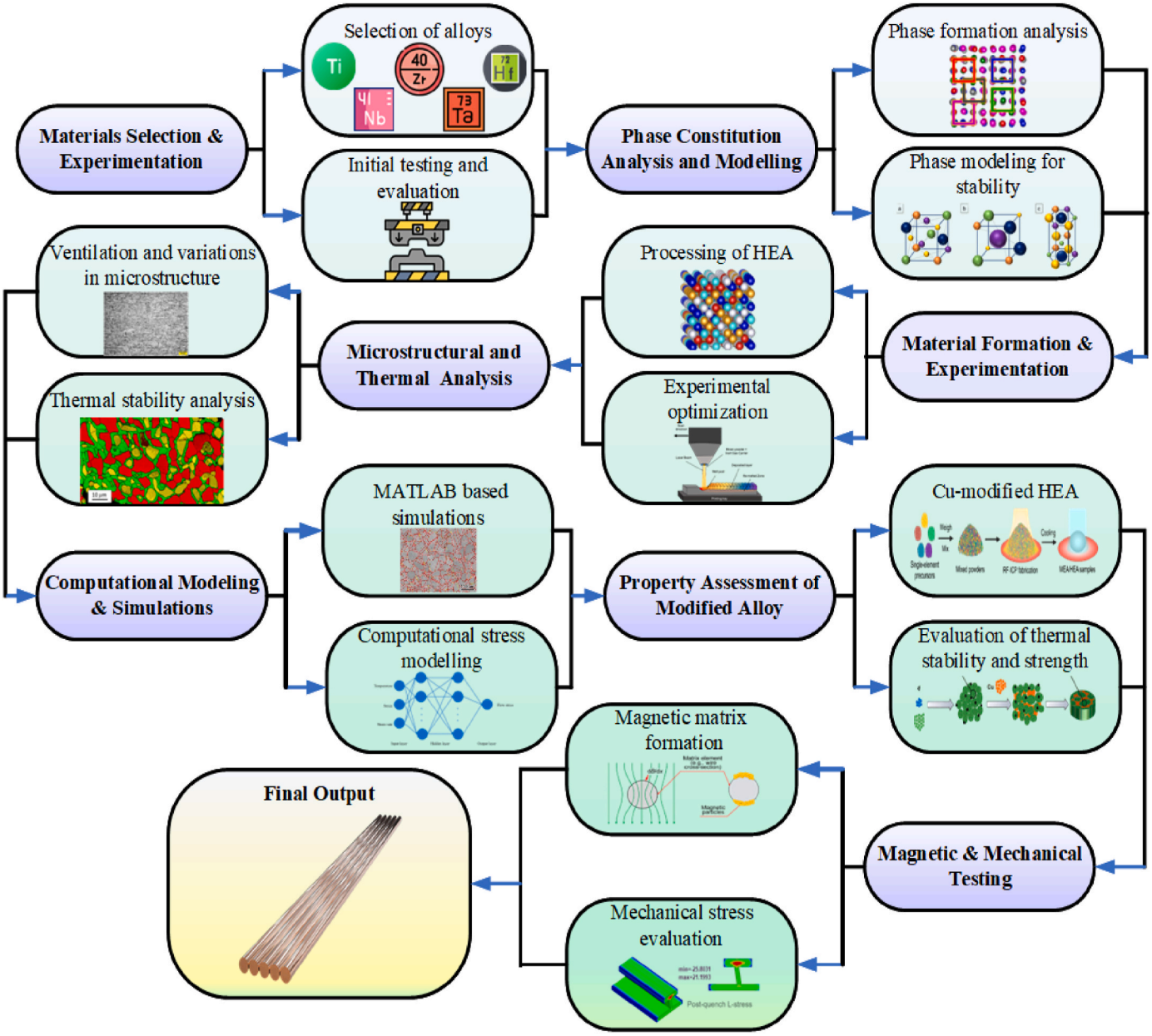

Fig. 1. Experimental workflow for Cu-modified Ti–Zr-Hf-Nb-Ta HEA.

The synthesis of high-entropy alloys (HEAs) is performed using powder metallurgy techniques to ensure compositional uniformity and structural integrity. Initially, high-energy ball milling is employed to achieve thorough blending of the elemental powders. This is followed by uniaxial compaction, where the blended powders are pressed into pellets under controlled pressure. The compacts are then sintered in an inert or vacuum environment to prevent oxidation and promote densification. Careful optimization of sintering parameters such as temperature, applied pressure, and dwell time is undertaken to ensure high density, minimal porosity, and uniform phase distribution within the sintered HEAs.

❖ **Microstructural and Thermal Analysis**

- Microstructural Analysis: X-ray diffraction (XRD) is employed to identify phase structures and lattice parameters.
- Thermal Stability: Thermogravimetric analysis (TGA) and differential scanning calorimetry (DSC) are used to assess thermal degradation temperatures and stability across the Cu composition range.

Changes in grain size, lattice strain, and phase morphology due to Cu addition are studied in detail.

❖ **Computational Modelling & Simulations**

MATLAB-based simulations are employed to complement experimental observations and predict the behavior of the copper-modified HEAs under various conditions. Phase field modeling is utilized to simulate the microstructural evolution, capturing phenomena such as grain coarsening, phase separation, and the development of secondary phases. Finite Element Analysis (FEA) is conducted to evaluate stress distribution, predict microcrack propagation, and assess thermal expansion behavior under simulated operational environments. Together, these computational tools provide critical insights into optimizing alloy compositions and forecasting real-world mechanical and thermal performance.

❖ **Property Assessment of Modified Alloy**

This phase focuses on evaluating the direct effect of copper content on the structural and mechanical performance of the alloy. Mechanical testing, including compression tests and Vickers microhardness measurements, is performed to assess yield strength, ductility, and hardness. Structural analysis investigates lattice distortion and solid solution effects, correlating them with the mechanical response. The observed changes in microstructure due to copper addition are systematically linked to variations in mechanical integrity, identifying both enhancements and compromises in performance.

❖ **Magnetic & Mechanical Testing**

The magnetic characteristics of the HEAs are studied in parallel with mechanical evaluations:

- Magnetic Testing: Parameters like saturation magnetization and Curie temperature are determined using vibrating sample magnetometry (VSM).
- Mechanical Stress Evaluation: Stress-strain behaviour and crack initiation are assessed to ensure mechanical resilience under loading.

This dual testing phase highlights compositions that offer balanced magnetic sensitivity and mechanical strength.

❖ **Final Output**

The optimized copper-modified HEA demonstrates a balanced combination of enhanced mechanical strength, thermal stability, and tunable magnetic properties. Developed through integrated experimental and computational methods, the alloy exhibits a refined microstructure and improved phase stability. Its multifunctionality makes it ideal for structural and functional applications. Potential use cases include aerospace components, magnetic shielding systems, and advanced engineering applications.

The density of the sintered HEA specimens is determined following Archimedes' principle. The specimen's density is calculated in accordance with ASTM B962-14 standards, utilizing the specified equation (1).

$$\rho = \frac{M_{dry}}{M_{dry} - M_{sub}} \tag{1}$$

where, ρ represents the density of the specimen $\left(g/cm^3\right)$, M_{dry} denotes the mass of the specimen in air and M_{sub} denotes the mass of the specimen when fully submerged in water. The experiment is conducted with three repetitions to ensure precision and validate the consistency of the results. The alloy's theoretical density (ρ_{calc}) is measured based on Equation (2).

$$\rho_{calc} = \sum Y_j \rho_j \tag{2}$$

where, Y_j represents the weight fraction of the j^{th} element in the alloy, ρ_j represents the density of the j^{th} pure element $\left(g/cm^3\right)$.

The compaction efficiency is determined using Equation (3).

$$D_{eff} = \frac{\rho_{measured}}{\rho_{pred}} \times 100\% \tag{3}$$

where D_{eff} and ρ_{pred} denote the observed and calculated densities, $\rho_{measured}$ represents the measured density of the sintered alloy specimen $\left(g/cm^3\right)$, respectively. The porosity percentage (p) is determined using Equation (4).

$$P\% = \left(\frac{\rho_{pred} - \rho_{measured}}{\rho_{pred}}\right) \times 100\% \tag{4}$$

The phase structure and composition of the Ti–Zr-Hf-Nb-Ta HEA samples are analyzed using XRD. The systematic examination is done with the help of XRD with CuKα radiation operating at 15 mA and 40 kV [31]. The William-Hall formula is utilized to analyze the crystal size of the HEA samples, under the given equation.

$$X = \frac{K \cdot \lambda}{L \cdot \cos(\alpha)} \tag{5}$$

where, crystal size (X), Shape factor (K), full width at half maximum (L), peak position (α), and wavelength (λ) that are related in the above equation define the crystal's structural characteristics. Subsequently, the lattice strain (ε) is determined by a specific equation.

$$\delta = \frac{\alpha}{4 \tan \varphi} \tag{6}$$

The lattice constant is determined using the following equation

$$b^2 = \frac{m^2}{(n^2 + p^2 + q^2) \cdot (2 \cdot \sin \gamma)^2} \tag{7}$$

where, b represents the Lattice constant, indicating the unit cell dimension of the crystal structure, m represents the order of reflection, Miller indices of the crystallographic plane are denoted as n, p, q , the Bragg angle is denoted as γ.

The dislocation density of the HEA powder is determined using the following equation:

$$\rho_d = k \cdot \sqrt{\langle \varepsilon^2 \rangle} \cdot \frac{1}{D} \tag{8}$$

where, ρ_d represents the dislocation density, k represents the constant, ⟨

$\varepsilon^2\rangle$ represents the mean squared strain, D represents the average crystallite size. The energy equation is the fundamental equation governing heat transfer in a time-dependent system. This equation is given by:

$$\eta\phi\frac{d\Theta}{d\tau} = -\nabla\cdot J + \Psi \tag{9}$$

where, η denotes the mass density, ϕ denotes the heat capacity, Θ denotes the temperature, τ denotes the time, J represents the heat flux vector, Ψ denotes the internal heat generation term. Fourier's Law on the conduction of heat is stated as:

$$J = -\lambda\nabla\Theta \tag{10}$$

where, λ represents the effective thermal conductivity, $\nabla\Theta$ represents a temperature gradient. The model for laser power distribution is designed in two distinct ways for comparison purposes.

$$\dot{J}''_{uniform} = \frac{W}{\pi R_0^2} \tag{11}$$

$$\dot{J}''_{spherical} = \frac{3Q}{2\pi R_0^2}\sqrt{\left|1 - \frac{(X-X_0)^2}{R_0^2} - \frac{(Y-Y_0)^2}{R_0^2}\right|} \tag{12}$$

where, $\dot{J}''_{uniform}$ represents the heat flux, W represents the total energy input, R_0 represents the radius of the circular heating area, $\dot{J}''_{spherical}$ represents the heat flux for the spherical case, Q represents the total applied energy, X, Y represents the coordinates in the heating region, X_0, Y_0 represents the center coordinates of the heating area. For the other boundary conditions of heat transfer, the account for convective and radiative heat losses from the upper surface. The radiative heat loss from the surface is given by the Stefan-Boltzmann Law.

$$\dot{J}''_{rad} = \alpha\varsigma\left(T_1^4 - T_0^4\right) = h_{rad}(T_1 - T_0) \tag{13}$$

where, $\dot{J}''_{rad}$ represents the radiative heat flux, α represents the new emissivity, ς represents the new constant associated with the Stefan-Boltzmann constant, T_1 denotes the new surface temperature, T_0 denotes the new ambient temperature, h_{rad} denotes the radiative heat transfer coefficient. The loss in convection from the surface is stated in the following equation:

$$\dot{J}''_{conv} = h_c(T_s - T_\infty) \tag{14}$$

where, $\dot{J}''_{conv}$ denotes the Convective heat flux, h_c denotes the convective heat transfer coefficient, T_s denotes the Surface temperature, T_∞ denotes the ambient fluid temperature.

In this research, an almost quasi-static mechanical analysis is given for temperature dependence. This is carried out in the event of layer deposition upon layer under controlled ambient conditions, to identify the stress-deformation behaviour. Thus, the basic relevant stress distribution equation is:

$$\nabla\cdot\tau = 0 \tag{15}$$

where, the stress tensor is denoted by τ. For the Ti–Zr-Hf-Nb-Ta alloy, which exhibits minimal hardening once the stress surpasses the yield strength, a common approach is to use a perfectly plastic model. This model assumes that the material behaves elastically up to the yield point, and after reaching the yield strength, it undergoes perfectly plastic deformation with no further increase in stress [32]. The constitutive law for this behaviour is typically expressed as:

$$\tau = A : \xi_e \tag{16}$$

$$\varsigma = \xi_p + \xi_f \tag{17}$$

where, A represents the material's stiffness matrix, denotes the elastic strain, ς denotes the total strain, ξ_p represents the plastic strain, ξ_f denotes the phase change strain. The thermal strain due to isotropy is calculated as:

$$\varsigma_T = \lambda T_K \tag{18}$$

$$\lambda_T = \theta(T - T_{base}) \tag{19}$$

where, λ represent the material property constant, T_K represent the reference temperature, θ represent the coefficient of thermal expansion, T represent the temperature, and T_{base} represent the base temperature. Residual stress is determined from the stress tensor by applying the Von Mises stress criterion. The yield function is then evaluated as

$$\varphi = \tau VM - \tau Y \tag{20}$$

where, φ represents the yield function, τVM denotes the Von Mises stress, τY denotes the yield stress. The initial yield stress, τ_{Y0} represent the temperature-dependent quantity. Therefore, it varies with temperature as follows:

$$\tau_Y(T) = \tau_{Y0}(T) \tag{21}$$

where, $\tau_Y(T)$ represents the temperature-dependent critical stress, $\tau_{Y0}(T)$ represents the reference critical stress at temperature T. In the elastic region, the elastic modulus is influenced by the local temperature. The microstructures of HEAs are typically composed of solid-solution phases, due to their high entropy. This high entropy prevents the formation of intermetallic compounds and enhances the solubility of additional elements. In HEAs where each element is present in an equimolar proportion, the configurational entropy grows logarithmically as the amount of components increases, as described by the following equation:

$$S = R\cdot\ln(N) \tag{22}$$

where, S denotes the configurational entropy, R denotes the universal gas constant, N denotes the number of components in the alloy. High-entropy solid-solution phases arise from the increased entropy, which is greater than that in conventional alloys. This phenomenon is explained by the Gibbs free energy of mixing (ΔG_m) for a solid-solution phase [33].

$$\Delta G_m = \Delta E_x - T\Delta Q_x \tag{23}$$

where, ΔE_x represents the change in energy, T represents the temperature, ΔQ_x represents the change in entropy.

3. Results and discussions

This section analyses the effect of varying copper content on the mechanical properties, phase constitution, and magnetic behavior of Ti–Zr-Hf-Nb-Ta HEA. MATLAB simulation phase change; hardness; yield strength; ductility; and magnetic properties are investigated for optimal copper content for enhanced performance.

The ΔG_{mix} in kJ mol^{-1} is plotted against the molar ratio of copper to Ti–Zr-Hf-Nb-Ta at all stated temperatures of 250 K, 500 K, 750 K, 1250 K, and 1750 K in Fig. 2. The ΔG_{mix} values range roughly between −3.5 and −0.5 kJ/mol, and the curves mostly increase with increasing Cu/Ti–Zr-Hf-Nb-Ta values. At greater temperatures, curves increase more sharply showing a pronounced dependence of mixing energy on composition with temperature. Temperature effect is seen, with less negative ΔG_{mix} values corresponding to higher temperatures, indicating that mixing becomes less favorable under these thermal conditions. This highlights the critical role temperature plays in tuning the thermodynamic stability of the alloy system.

Fig. 3(a) illustrates the XRD pattern of HEA-1. For the diffraction peaks detected at about 50.5°, 60.2°, and 85.2°, it is clear that the material possesses a well-defined crystalline structure. The most intense

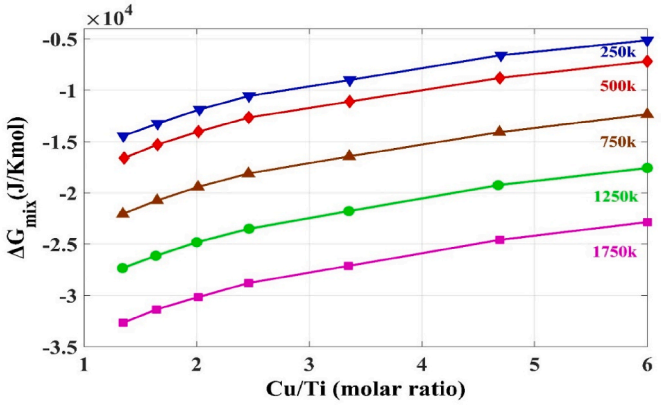

Fig. 2. The dependence of ΔG_{mix} on the (Cu/Ti) molar ratio at a specific temperature in the Ti–Zr-Hf-Nb-Ta HEA.

peak of about 50.5° at 210 a.u indicates there is a strong preferred orientation in that phase. The sharpened peaks indicate stabilization of phase while having a minimal amorphous content. This pattern confirms the formation of a single-phase structure, which is favorable for achieving uniform mechanical and thermal properties.

Fig. 3(b) depicts the XRD pattern of HEA-2. The peaks appear at 50.7°, 61.0°, and 86.0°. The most prominent peak is found to be 220 a.u at 50.7°. The peaks seem a bit broader as compared to the HEA-1, possibly due to some refinement in the grain size or slight lattice strain. The general intensity is seen to be on par with the other HEAs, thus implying a stable phase. This change suggests that Si acts as a microstructural modifier, influencing crystallite size and inducing slight distortions in the lattice.

Fig. 3(c) presents the XRD pattern of HEA-3. The peaks are positioned at 50.6°, 60.7°, and 85.8°, while the maximum intensity is 50.6° at 230 a.u. The sharpness of the peak suggests a very high crystallinity. The phase formation is similar to that of HEA-1 and HEA-2. The positions of the peaks point towards a face-centred cubic structure, which is as other HEAs. The improved sharpness indicates enhanced crystallinity, while the introduction of Cu may have reinforced the FCC lattice without introducing additional phases.

Fig. 3(d) shows the XRD pattern for HEA-4. All the diffraction peaks are noted at 54.8°, 61.2°, and 86.4°, corresponding to the similar previous samples. The highest peak intensity, 240 a.u at 54.8°, indicates dominance of the concerned phase. Moderation in the peak broadening is still experienced, which, however, now slightly varies when compared with the case of HEA-3. This suggests a synergistic influence of both Si and Cu in stabilizing the crystalline structure, possibly affecting the solid solution strengthening mechanisms.

Fig. 3(e) compares the XRD pattern of the proposed alloy. The diffraction peaks occur at 54.5°, 61.5°, and 86.7°. Here, 250 a.u at 54.5° is the peak intensity maximum among all the peaks of the obtained HEAs. Compared to others, the peaks are sharper with higher intensity; thus, the proposed material generates the best-defined structure with higher peak intensity, suggesting better phase purity and probably good mechanical strength. The proposed alloy in Fig. 3(e) gives the highest intensity peaks and the most stable phase structure, presenting the greatest promise among the HEAs. This improvement indicates the proposed composition achieves optimal atomic packing and phase stability, which may directly correlate with improved mechanical

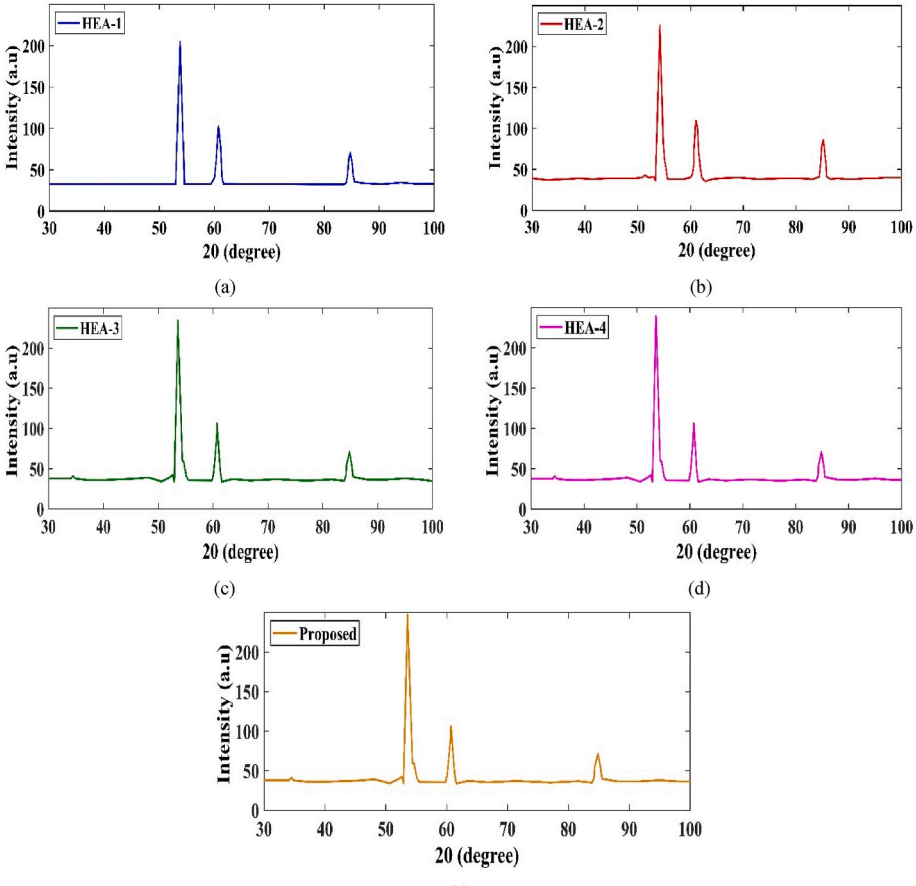

Fig. 3. XRD analysis of different high-entropy alloys (a) HEA 1 (Fe2CoCrNi0.5), (b) HEA 2 (Fe2CoCrNi0.5Si0.25), (c) HEA 3 (Fe2CoCrNi0.5Cu0.25), (d) HEA 4 (Fe2CoCrNi0.5Si0.25Cu0.25), and (e) proposed.

performance and structural integrity.

Fig. 4 shows the mass loss per unit area (Δm/A in mg cm^{-2}) as a function of time for up to 1200 h on HEA-1, HEA-2, HEA-3, HEA-4, and the proposed material. The rate of degradation in HEA-3 is maximum, more than 15 mg cm^{-2}, then HEA-4 and HEA-2 show a degradation trend, whereas HEA-1 maintains low mass loss; however, that is also higher than 5 mg cm^{-2}. The proposed material has the lowest mass loss, remaining below 5 mg cm^{-2} throughout the test. This represents that the proposed alloy is more stable and resistant to wear than other HEAs, thus being a potential candidate for applications requiring corrosion resistance and high durability. These results demonstrate the superior oxidation resistance of the proposed alloy under prolonged exposure conditions.

Fig. 5(a) illustrates a material system with temperature where the phase composition of FCC remains nearly 100 % below approximately 820 °C. As the temperature increases beyond 820 °C, the FCC phase rapidly drops down to 0 %, while the liquid phase correspondingly rises to nearly 100 % by around 860 °C. This change in phase signals an important solid-to-liquid phase transition within this temperature range. Additionally, the Laves phase remains constant at around 10 % up to 820 °C before disappearing completely beyond this point. This transition range is critical for understanding the melting behavior and thermal stability of the alloy, as it defines the upper limit for solid-state applications.

Fig. 5(b) shows the composition of the phase of the material system in terms of temperature, represented as mole percent for the liquid phase, the FCC phase, and laves phase. At temperatures less than 700 °C, the FCC phase is clearly dominant at about 80 %, while the liquid phase is minimal. When the temperature approaches about 800 °C, the FCC phase plummet to 0 %, and the liquid phase shoots up to nearly 100 %. The laves phase occurs typically around 750 °C while showing a limited occurrence, slowly rising with a temperature increase. The emergence and disappearance of phases around transitional temperatures suggest that minor compositional or thermal fluctuations can significantly influence microstructural stability.

Fig. 5(c) represents the composition of a phase of a material system over temperature from 400 °C up to 900 °C; the mole percentage is shown in the liquid, FCC, and laves phase. Below around 700 °C, it shows that the FCC phase holds steady at approximately 80 % and the liquid phase is a small percentage. As the temperature continues to increase past 800 °C, the FCC phase drops rapidly to 0 %, and the liquid phase increases to nearly 100 %. The laves phase is seen at around 750 °C, which increases slightly before stabilizing with temperature. This behavior underlines the thermal sensitivity of the alloy system and the role of metastable phase formation in high-temperature environments.

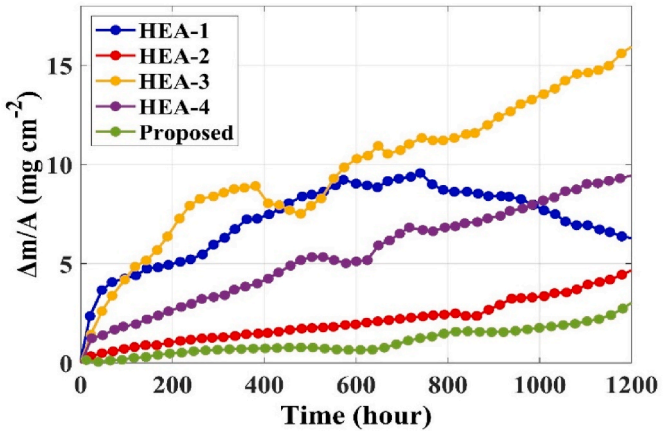

Fig. 4. The variation of mass change per unit surface area of HEAs with oxidation time.

Fig. 5(d) represents the phase composition of a material system in terms of temperature with the mole percentages of the liquid phase, FCC phase, and laves phase. At temperatures less than 700 °C, the FCC phase remains relatively stable at around 60 % with the liquid phase beginning near 0 %. The FCC phase diminishes to approximately 0 % as the temperature approaches 800 °C. In this same range, the liquid phase is increased to approximately 90 %. The laves phase starts appearing at around 750 °C, which steadily increases and goes up to around 40 % at 900 °C. This gradual increase in the Laves phase content suggests a stronger tendency for intermetallic phase stabilization, which may impact the alloy's mechanical properties and brittleness at elevated temperatures.

Fig. 5(e) illustrates the phase composition of a material system between 600 °C and 900 °C, with mole percentages for the liquid phase, FCC phase, and laves phase. At temperatures below 700 °C, the FCC phase is at around 70 %, and the liquid phase is at a very low value of about 10 %. When the temperature increases to 800 °C, the laves phase falls to 0 % very quickly, and the liquid phase is at about 90 %. The FCC phase appears at around 750 °C, gradually increasing to about 30 % by 900 °C. This unusual reformation of the FCC phase at higher temperatures could indicate a secondary solidification process or re-precipitation behavior influenced by specific compositional balancing in the proposed alloy.

Fig. 6 illustrates microhardness (HV0.5) measurements taken of some materials Ti, Zr, Hf, Nb, and Ta, as a function of distance from the surface in millimetres from 0 to 50 mm. From a distance of 20 mm, the microhardness values of about 450 H0.5 for Ti and about 400 HV0.5 for Zr seem reachable. At a distance of about 40 mm, microhardness is seen to have dropped in all the materials. The values become stable at between 100 and 150 HV0.5 by 50 mm. This trend indicates that microhardness decreases dramatically near the surface and then levels off at larger distances, revealing the effects of processing or structural changes in the materials. This behavior underscores the significant influence of surface treatments on the mechanical properties of these alloys.

The average microhardness (HV0.5) of various alloys, Ti, Zr, Hf, Nb, and Ta, is represented in Fig. 7. The hardness of Ti is the lowest, around 300 HV0.5, whereas Zr increases a little to around 300 HV0.5. The average microhardness of Hf is relatively higher, reaching about 350 HV0.5. It increases further to about 400 HV0.5 for Nb, and the highest value among the alloys is for Ta, about 450 HV0.5. This trend shows that Ta has the highest resistance to indentation while Ti has the lowest, which explains the difference in their hardness. These results highlight the potential of Ta for applications requiring superior wear resistance and mechanical strength.

Fig. 8 represents magnetization (emu/g) vs the applied field (KOe) for the various compositions of FeCoNiCr, which are FeCoNiCr, $FeCoNiCr_{0.05}$, $FeCoNiCr_{0.1}$, $FeCoNiCr_{0.15}$, $FeCoNiCr_{0.2}$, and the proposed material. It is noted that the saturation magnetization curves vary with compositions and exhibit the typical ferromagnetic hysteresis characteristics. The proposed material has a maximum saturation magnetization at around ±100 emu/g for ±30 KOe. Other compositions have displayed different coercivities and saturation. Some of the compositions have high soft magnetic behavior. This indicates that the proposed material offers enhanced magnetic performance suitable for advanced magnetic applications.

Fig. 9 illustrates the variation of hardness (in HV) and yield strength (in MPa) with respect to increasing copper content (Cu wt%) in Ti–Zr-Hf-Nb-Ta high-entropy alloys. As the copper content increases from 0 % to 20 %, both hardness and yield strength exhibit a decreasing trend. At 0 % Cu, the hardness is approximately 200 HV, and the yield strength is around 670 MPa. With 5 % Cu, these values drop to 160 HV and 555 MPa, respectively. At 10 % Cu, the hardness reduces further to 140 HV, while yield strength reaches 510 MPa. For 15 % Cu, hardness is 118 HV, and yield strength is 460 MPa. Finally, at 20 % Cu, the lowest values are observed with 70 HV hardness and 380 MPa yield strength. This data clearly indicates that increasing Cu content leads to a reduction in both

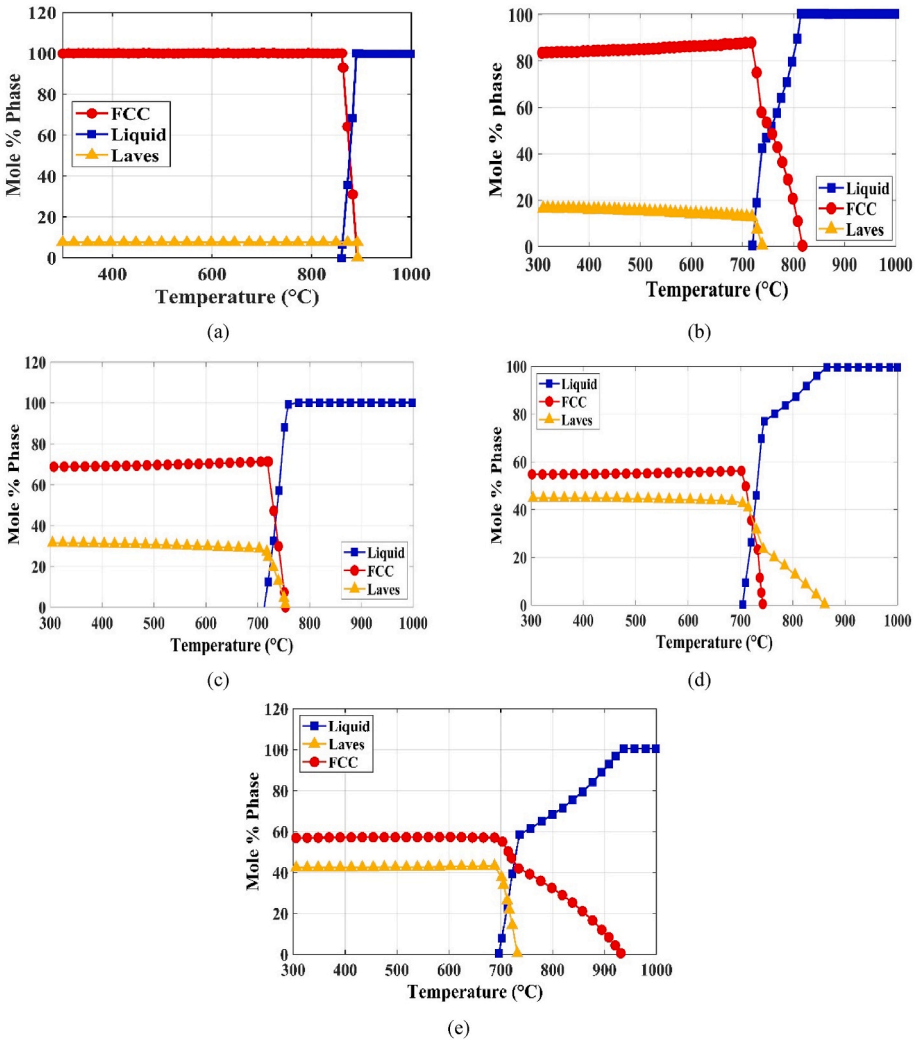

Fig. 5. Phase stability in HEA coatings: (a) Ti, (b) Zr, (c) Hf, (d) Nb, (e) Ta.

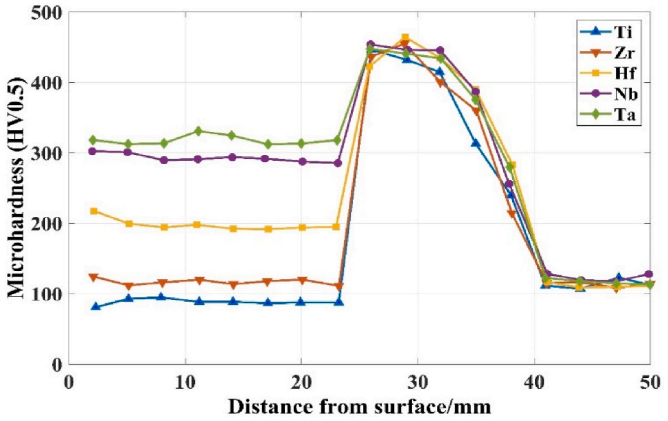

Fig. 6. Microhardness evaluation of the HEA coating.

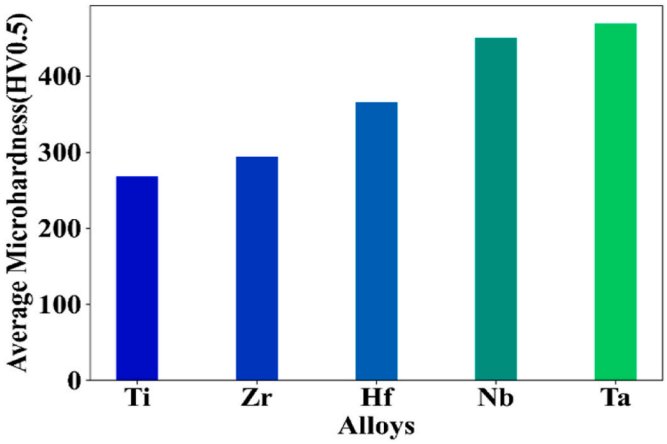

Fig. 7. Overall microhardness value.

hardness and yield strength.

Fig. 10 shows the coefficient of friction over time of the wave in minutes with various materials. Initially, for all of these materials at time 0 min, the friction coefficients are fairly low, around the value between approximately 0.1 and 0.3. At a wave time of 60 min, coefficients stabilize. Here, Ti remains the highest coefficient at around 0.7, while Ta is the least at approximately 0.4. The remaining Zr, Hf, and Nb showed intermediate behaviors in stabilizing to around 0.5–0.6. This result shows that there are differences between materials and, in general, Ti is observed to be much more resistant to sliding for the friction time. These results highlight the superior sliding resistance of Ti, making it a strong candidate for applications involving prolonged frictional contact.

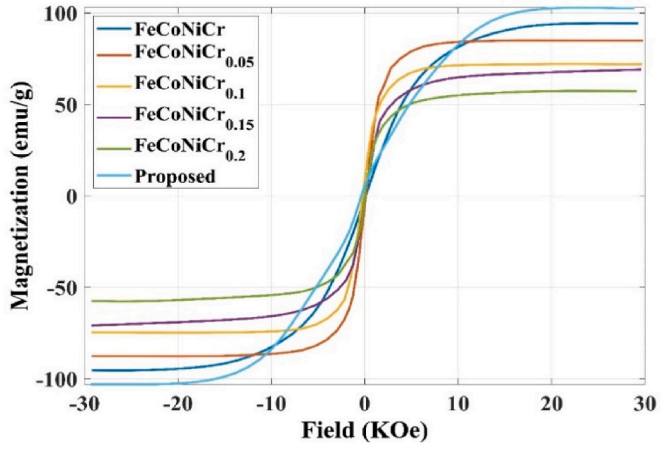

Fig. 8. Magnetization vs the field for different HEA compositions.

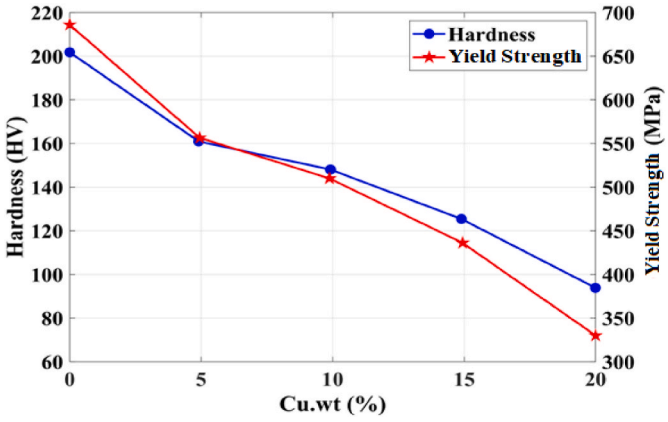

Fig. 9. Vickers macro hardness and yield strength characteristics of Ti–Zr-Hf-Nb-Ta HEAs.

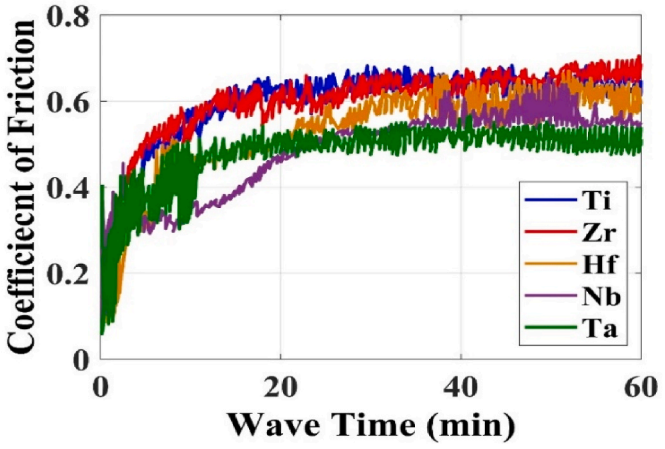

Fig. 10. Friction coefficient fluctuation curves of the coating.

Fig. 11 displays the average coefficient of friction of different alloys, namely Ti, Zr, Hf, Nb, and Ta. Ti has the lowest coefficient of friction at about 0.1, which means there is very little resistance to sliding. Zr increases to about 0.2. Hf further increases to about 0.4, while Nb reaches about 0.6, which shows a considerable increase in frictional resistance. Ta has the highest coefficient of friction at about 0.7. This trend has indicated that during the transition from Ti to Ta, the alloy's friction resistance increases significantly, while Ta poses maximum resistance to sliding. This clearly demonstrates the trade-off between hardness and frictional performance across the alloy series.

Fig. 12 displays the variation of 4πM (kG) vs. true field (KOe) for a variety of different material compositions that include Cu and Ti variations, FeCoNaAl, and the proposed material. Curves indicate the reaction of each of these compositions in an external magnetic field with varied coercivity and saturation magnetization. The material proposed has a well-defined hysteresis loop with a moderate coercivity, and compositions with modifications in Cu and Ti are showing different responses, which may be tuned for their magnetic properties. FeCoNaAl composition shows lower saturation magnetism, indicating a less intense ferromagnetic response. This suggests that compositional tuning provides a viable pathway to optimize the magnetic behavior of these HEAs for targeted applications.

Fig. 13 shows coercivity (Oe) as a function of annealing temperature (°C) for several Cu and Ti additions, FeCoNaAl, and the proposed material. This figure means that coercivity, defined as the strength of a material against demagnetization, depends strongly on annealing temperature. The maximum coercivity reaches even nearly 500 Oe for some compositions within 600–800 °C. The proposed material shows a relatively low coercivity, which is an indication of its soft magnetic nature. Other compositions show different trends, some with a huge increase in coercivity at higher temperatures. Therefore, the proposed material is the best in this case of soft magnetic properties. These results highlight the efficiency of the proposed alloy in maintaining desirable soft magnetic behavior across a broad thermal range.

Fig. 14 shows the hardness in terms of HV for different materials. The proposed method presents the highest hardness value, which is nearly 1000 HV. Therefore, it is the hardest material in the comparative research. CoCrFeNiAl has reached around 800 HV, and TiZrNbMo and TiZrNbMoW between 500 and 600 HV. Other examples are: the 17-4 PH stainless steel and Hastelloy around 300–500 HV. The lowest hardness recorded is the one experienced by the 316 stainless steels, less than 200 HV. The proposed method is the best since it registers the highest hardness, and thus the method suits wear-resistant applications. This exceptional hardness underscores the material's potential for demanding industrial uses where durability is critical.

Fig. 15 depicts tensile strength in MPa for various composite materials: alumina composites, boron-Ni trade composites, and the proposed material. For all four samples, the proposed material is seen to consistently obtain the largest tensile strength, indeed from 300 MPa up to more than 400 MPa, higher than those of boron-Ni trade composites (~300–380 MPa) and alumina composites (~250–350 MPa). Thus, it is the best of these comparisons, showing higher mechanical strength for all cases. This superior tensile strength highlights the proposed

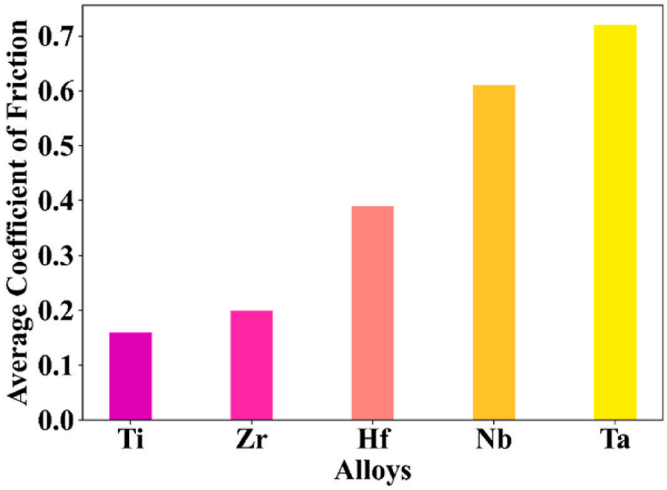

Fig. 11. Mean friction coefficient.

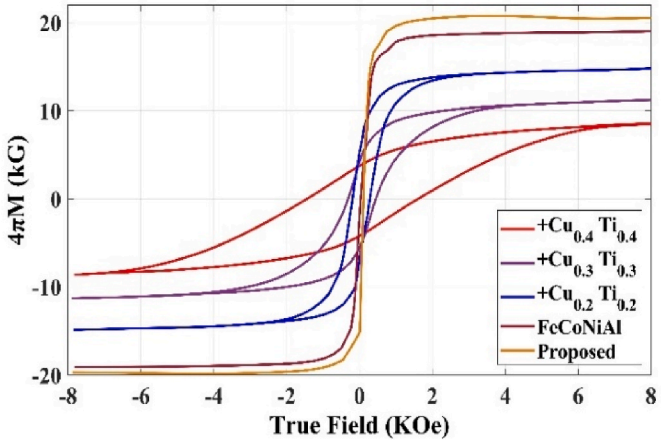

Fig. 12. Demagnetization loop for different HEA compositions.

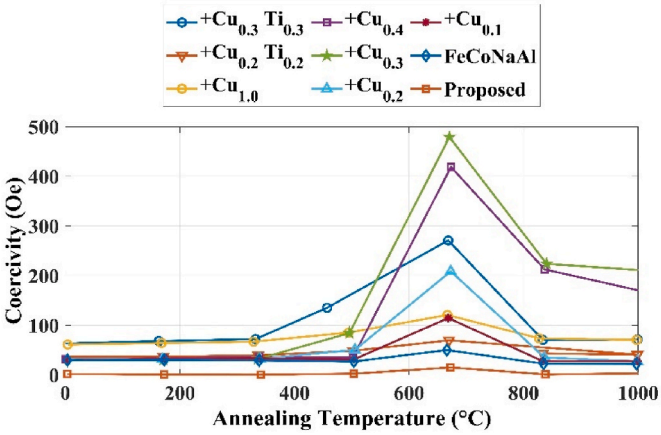

Fig. 13. The coercivity as a function of annealing temperature (°C) for various HEAs.

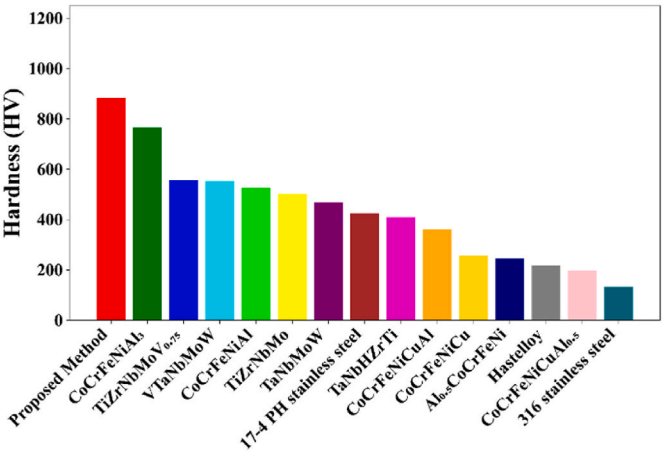

Fig. 14. Hardness comparison.

material's promise for structural applications demanding enhanced load-bearing capacity.

Fig. 16 shows the relationship between thermal strain, in 10^{-3} m/m with the temperature scale, in °C, between 0 and 400 °C. For a temperature of 0 °C, the corresponding thermal strain is around 0, essentially, meaning no deformation due to temperature variation. The increment of the temperature has correspondingly increased the thermal

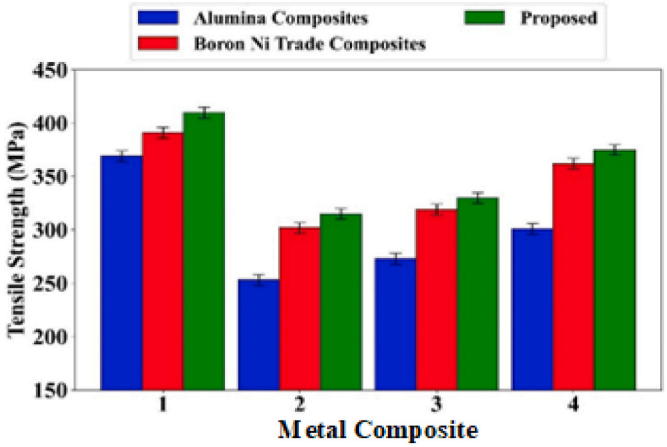

Fig. 15. Tensile strength comparison.

strain, which is about 2.5 at 400 °C. This gradual increase reflects the material's reaction to thermal expansion, which means that the material has a direct linear relationship between temperature and thermal strain within the measured range. The curve also shows that with higher temperatures, the material experiences greater thermal deformation. This linear behavior indicates predictable thermal expansion, important for designing components subjected to temperature fluctuations.

Fig. 17 demonstrates the stress-strain curve of various materials such as nickel, SS-304, SS-316, Ti-CP, Ti–6Al–4V, and proposed material. From the curve of the proposed material, the yield stress is highest, about 600 MPa, and for Ti–6Al–4V, strength is high, but lower than that of the proposed material. The curves for SS-304 and SS-316 for stainless steel and for nickel show relatively low values for stress and have a maximum at about 200–300 MPa. The proposed material is the best in this category, showing excellent mechanical strength with high ductility. This combination of strength and ductility makes the proposed material highly suitable for demanding structural applications.

Fig. 18 compares the corrosion rates of aluminium, copper, carbon steel, and the proposed alloy over 10 weeks: carbon steel had the highest corrosion rate, from about 25 mg cm^{-2} $year^{-1}$ up to almost 45 mg cm^{-2} $year^{-1}$, demonstrating rapid degradation of the material; copper similarly shows an increasing trend, indicating continuous corrosion; aluminium starts at about 12 mg cm^{-2} $year^{-1}$ but shows a gradual decrease, stabilizing at around 7 mg cm^{-2} $year^{-1}$ as a result of passive film formation, while the proposed alloy stayed at the low end of the corrosion rate at less than 5 mg cm^{-2} $year^{-1}$ for the entire investigation,

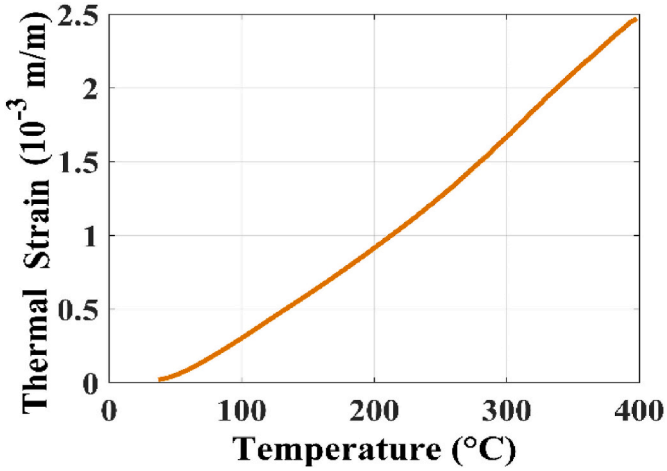

Fig. 16. Relationship between thermal strain (in 10^{-3} m/m) and temperature (°C).

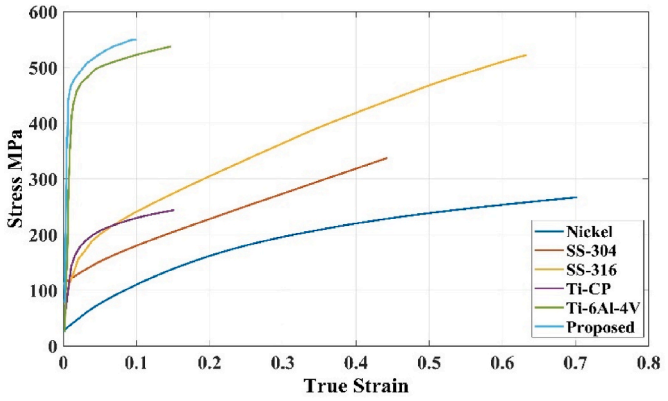

Fig. 17. The stress-strain relationship for different HEAs.

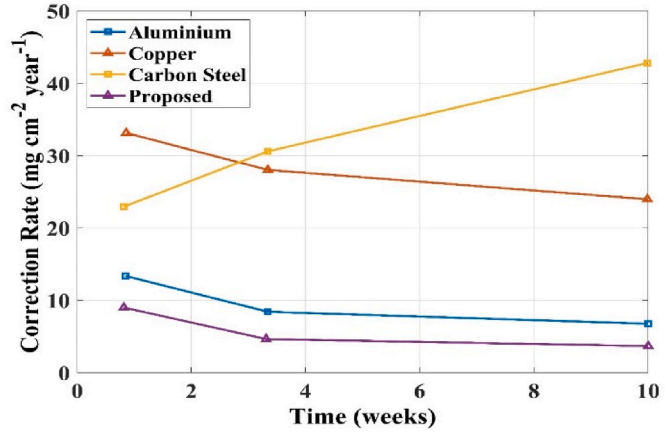

Fig. 18. The corrosion rate of different HEAs.

again showing very strong resistance to corrosion, which makes this an excellent candidate for use in harsh environments. This outstanding corrosion resistance significantly enhances the proposed alloy's suitability for long-term applications in aggressive conditions.

Fig. 19 depicts the material loss over 10 years for stainless steel (316), aluminum alloy (6061), titanium (Ti–6Al–4V), carbon steel, copper alloy (brass), and the suggested material. Carbon steel has the highest material degradation, which amounts to almost 1.8 mm loss. This shows carbon steel is the most prone to wear and corrosion. Copper alloy (brass) follows this with a constant increase in material loss, reaching more than 1 mm. Aluminum alloy (6061) and stainless steel (316) have a moderate performance with a consistent but slow material loss rate. Titanium (Ti–6Al–4V) and the proposed alloy show minimal material loss, which reflects their excellent durability and resistance to wear, and they are well suited for long-term structural applications. The low material loss of the proposed alloy underscores its potential for enhancing longevity in demanding environments.

Fig. 20 compares the magnetization curve as a function of applied magnetic fields for various references, namely Alnico (Al–Ni–Co–Fe), Permalloy (Ni–Fe), Stainless Steel (316), and the proposed material. The shape of the curve of magnetization for the proposed material approximates that of Alnico and Permalloy and is close to 1.0 magnetization at an applied field of 1.0 H. This suggests a strong ferromagnetic behavior identical to these commercially available magnetic materials. On the other hand, stainless steel (316) shows nearly zero magnetization, which supports its non-magnetic property. Since the proposed material behaves just like the other high-performance magnetic materials, such as permalloy and alnico but better than stainless steel (316), it is one of the best options in this comparison. This confirms the proposed material's

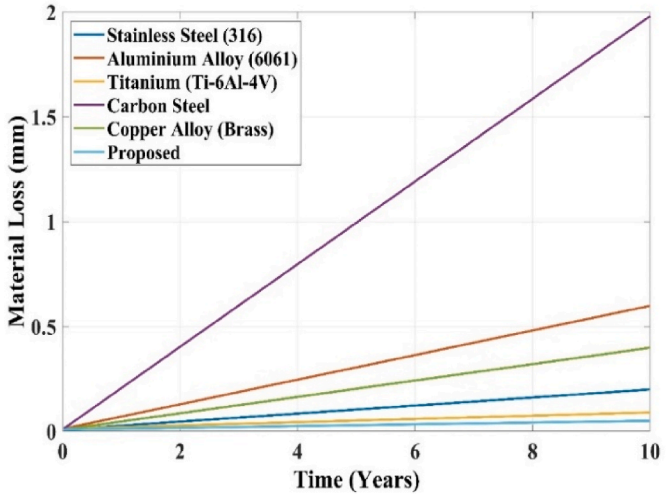

Fig. 19. The material loss over time for different alloys.

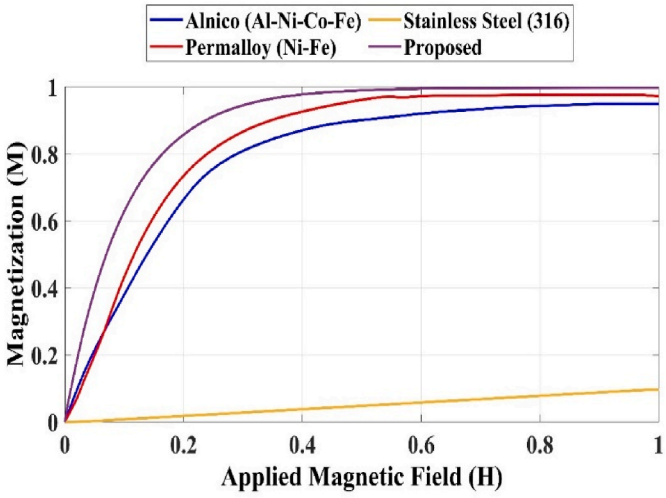

Fig. 20. Magnetization vs. Applied field.

potential as an effective alternative for advanced magnetic applications.

Table 1 compares the characteristics of five different alloys with reference to their hardness, theoretical density, and relative density. Hardness values vary from 236 ± 6 to 296 ± 6, the proposed alloy being the hardest at 296 ± 6. The theoretical densities of the alloys vary from 7.93 g/cm^3 to 8.53 g/cm^3, while their respective relative densities vary from 95.9 % to 98.76 %. Especially here, the alloy Fe2CoCrN0.5 shows hardness equal to 236 ± 6 and a relative density equal to 96.8 %. On the other hand, the proposed alloy shows the highest theoretical density, equal to 8.53 g/cm^3, and the highest relative density, equal to 98.76 %.

Table 1
Comparison of hardness and density in different alloys.

Alloy	Hardness	Theoretical density	Relative density
Fe2CoCrNi0.5Si0.25 [34]	261 ± 5	7.93	97.1
Fe2CoCrNi0.5 [34]	236 ± 6	8.09	96.8
Fe2CoCrNi0.5Si0.25Cu0.25 [34]	248 ± 5	8.14	95.9
Fe2CoCrNi0.5Cu0.25 [34]	269 ± 6	7.99	96.4
Proposed	296 ± 6	8.53	98.76

4. Conclusion

The research shows that the varying content of copper in Ti–Zr-Hf-Nb-Ta HEAs significantly impacts its phase constitution, mechanical properties, thermal stability, and magnetic behaviour. A significant change in microstructure has been observed for increasing copper content (0–20 %), from the formation of copper-rich regions and secondary phases that change the response of the alloy to external stimuli. These microstructural evolutions are correlated to decreasing mechanical performance, where both hardness and yield strength decrease, indicating that the incorporation of copper weakens the load-bearing capacity while influencing the material's structural integrity. The obtained results show as well that copper addition enhances thermal stability, stabilizes corresponding phases, and increases degradation temperatures, which may be important for high temperature applications. In addition, the modification of magnetic properties of the alloy by copper is also found, in which saturation magnetization and curie temperature are varied. The effects of segregation of copper showed a significant influence on the ferromagnetic behavior and pointed towards possible applications in areas where both mechanical strength and magnetic sensitivity are simultaneously required. This research provides the first comprehensive analysis of Cu-doped Ti–Zr-Hf-Nb-Ta HEAs synthesized via powder metallurgy, bridging existing gaps in understanding the correlation between Cu content and multifunctional performance. The optimal range of copper content (10–20 %) indicated good balance between enhanced strength, thermal stability, and magnetic performance. These results open new avenues for the design of advanced HEAs, with applications ranging from structural components to functional materials in various industries, including aerospace, electronics, and energy. Future investigations should incorporate long-term fatigue, corrosion behavior, and multi-objective optimization models to fine-tune Cu composition for application-specific needs. The future research needs to look into optimizing the content of copper in Ti–Zr-Hf-Nb-Ta HEAs, thereby refining their mechanical, thermal, and magnetic properties. Long-term stability, environmental performance, and advanced modeling would be necessary for further improvements in their industrial applications.

Ethical approval

All applicable institutional and/or national guidelines for the care and use of animals were followed.

CRediT authorship contribution statement

Md. Ahasan: Validation, Conceptualization, Methodology. **Kiran Kumar Billa:** Supervision, Visualization, Project administration. **Gollapalli Veera Satya Srinivas:** Formal analysis, Data curation, Funding acquisition. **D.S. ChandraMouli:** Investigation, Visualization, Supervision. **R.S. Srikanth Varma:** Resources, Methodology, Data curation. **P. Sri Gowri Padmaja:** Writing – original draft, Software, Formal analysis. **Rama Bhadri Raju Chekuri:** Supervision, Writing – review & editing, Funding acquisition. **Gattem Naga Lakshmi:** Methodology, Validation, Resources.

Informed consent

For this type of analysis formal consent is not needed.

Data availability statements

Data sharing not applicable to this article as no datasets were generated or analyzed during the current study.

Funding

This research did not receive any specific grant from funding agencies in the public, commercial, or not-for-profit sectors.

Declaration of competing interest

The authors declare that they have no known competing financial interests or personal relationships that could have appeared to influence the work reported in this paper.

Acknowledgement

None.

Data availability

No data was used for the research described in the article.

References

[1] D. Lakhdari, N. Lakhdari, I. Laourari, A. Berchi, Y. Park, Y. Vasseghian, et al., Bimetallic composite catalyst based on NICU alloy supported on PVA/Pani film polymer for electrodegradation of methanol, J. Ind. Eng. Chem. 124 (2023) 422–430, https://doi.org/10.1016/j.jiec.2023.04.037.

[2] S.P. Dwivedi, S. Sharma, A.P. Srivastava, V.A. Sethi, K.A. Mohammed, A. Kumar, et al., Homogeneity, metallurgical, mechanical, wear, and corrosion behavior of ni and b4c coatings deposited on 304 stainless steels developed by microwave cladding technique, J. Mater. Res. Technol. 27 (2023) 5854–5867, https://doi.org/10.1016/j.jmrt.2023.10.202.

[3] B. Singh, I. Kumar, K.K. Saxena, K.A. Mohammed, M. Ijaz Khan, S. Ben Moussa, et al., A future prospects and current scenario of aluminium metal matrix composites characteristics, Alex. Eng. J. 76 (2023) 1–17, https://doi.org/10.1016/j.aej.2023.06.028.

[4] H. Ahmadian, T. Zhou, M. Abd Elaziz, M. Azmi Al-Betar, A.M. Sadoun, I.M. R. Najjar, et al., Predicting crystallite size of mg-ti-sic nanocomposites using an adaptive neuro-fuzzy inference system model modified by termite life cycle optimizer, Alex. Eng. J. 84 (2023) 285–300, https://doi.org/10.1016/j.aej.2023.11.009.

[5] Y. Huang, J. Gao, S. Wang, D. Guan, Y. Xu, X. Hu, et al., Influence of tantalum composition on mechanical behavior and deformation mechanisms of tizrhftax high entropy alloys, J. Alloys Compd. 903 (2022) 163796, https://doi.org/10.1016/j.jallcom.2022.163796.

[6] S.P. Dwivedi, S. Sharma, C. Li, Y. Zhang, A. Kumar, R. Singh, et al., Effect of nano-tio2 particles addition on dissimilar AA2024 and AA2014 based composite developed by friction stir process technique, J. Mater. Res. Technol. 26 (2023) 1872–1881, https://doi.org/10.1016/j.jmrt.2023.07.234.

[7] S. Liang, Y. Zhou, L. Yin, Strengthening/weakening action of zr on stabilizers of TI alloys and its effect on phase transition, J. Mater. Eng. Perform. 30 (2021) 876–884, https://doi.org/10.1007/s11665-020-05408-2.

[8] H.K. Garg, S. Sharma, R. Kumar, A. Manna, S.P. Dwivedi, M. Abbas, et al., Mechanical, tribological, and morphological properties of SiC and GR reinforced Al-0.7Fe-0.6Si-0.375Cr-0.25ZN based stir-casted hybrid metal matrix composites for automotive applications: fabrication and characterizations, J. Mater. Res. Technol. 28 (2024) 3267–3285, https://doi.org/10.1016/j.jmrt.2023.12.171.

[9] G. Keskin, S. Salunkhe, G. Küçüktürk, M. Pul, H. Gürün, V. Baydaroğlu, Optimization of PMEDM process parameters for B4C and B4C+sic reinforced AA7075 composites, J. Eng. Res. (2023), https://doi.org/10.1016/j.jer.2023.09.012.

[10] Z. Wang, Y. Yan, Y. Wu, X. Huang, Y. Zhang, Y. Su, et al., Corrosion and tribocorrosion behavior of equiatomic refractory medium entropy tizr(hf, Ta, NB) alloys in chloride solutions, Corros. Sci. 199 (2022) 110166, https://doi.org/10.1016/j.corsci.2022.110166.

[11] S.A. Shanmuga Priya, P. Srivastava, G.V. Srinivas, S. Banerjee, A. Fatehmulla, A. C. Haldar, Enhanced oxygen evolution reaction via CuO@N-doped carbon nanostructures: a facile synthesis and electrocatalytic investigation, Res. Chem. Intermed. 51 (2025) 923–937, https://doi.org/10.1007/s11164-024-05465-5.

[12] C. Li, X. Xia, J. Cai, Z. Zhang, J. Wang, Z. Qian, et al., Influence analysis of B4C content on the neutron shielding performance of B4C/AL, Radiat. Phys. Chem. 204 (2023) 110684, https://doi.org/10.1016/j.radphyschem.2022.110684.

[13] S.L. Li, P. Hu, T. Liu, Q.-S. Shi, B.-L. Hu, X.-J. Hua, et al., Micro-nano secondary phase greatly increases the plasticity of titanium-zirconium-molybdenum alloy, Int. J. Refract. Metals Hard Mater. 112 (2023) 106152, https://doi.org/10.1016/j.ijrmhm.2023.106152.

[14] P. Bharathi, T.S. kumar, Mechanical characteristics and wear behaviour of Al/Sic and al/sic/b4c hybrid metal matrix composites fabricated through powder metallurgy route, Silicon 15 (2023) 4259–4275, https://doi.org/10.1007/s12633-023-02347-0.

[15] A. Saxena, S.P. Dwivedi, A.K. Srivastava, A. Kaushik, S. Sharma, Micro-mechanical finite element analysis on mechanical behavior of EN31 steel-based metal matrix

composite, Trans. Indian Inst. Met. 76 (2023) 685–694, https://doi.org/10.1007/s12666-022-02691-6.
[16] D. Yan, K. Song, H. Sun, S. Wu, K. Zhao, H. Zhang, et al., Microstructures, mechanical properties, and corrosion behaviors of refractory high-entropy retawnbmo alloys, J. Mater. Eng. Perform. 29 (2020) 399–409, https://doi.org/10.1007/s11665-019-04540-y.
[17] V.A. Kondapalli, K. Suresh, M. Ramakrishna, N. Narasaiah, B. Srinivasarao, Effect of cu content on the microstructure and mechanical properties of Fenimncuxal0.1Ti0.1 (x = 0.5,1.0 and 1.5) high entropy alloy system, J. Alloys Compd. 940 (2023) 168819, https://doi.org/10.1016/j.jallcom.2023.168819.
[18] Q. Wang, Q. Hu, H. Wang, L. Zeng, Investigations on the microstructures and tribological behaviors of AS-cast crfeconicux high entropy alloys, Intermetallics 157 (2023) 107886, https://doi.org/10.1016/j.intermet.2023.107886.
[19] J. Chen, T. Xiang, W. Bao, B. Yu, J. Li, Y. Wang, et al., Novel strength-electrical conductivity synergy in CU-based composites reinforced with tizrnbta high entropy alloy, Mater. Sci. Eng. 878 (2023) 145210, https://doi.org/10.1016/j.msea.2023.145210.
[20] Y. Liu, N. Tan, Y. Li, G. Zhang, W. Yin, G. Li, et al., Microstructure, hardness, and tribological properties of cocrfenix (x = mo, tiw) high entropy alloy coating by red-blue composite laser cladding on copper alloy, Surf. Coating. Technol. 483 (2024) 130761, https://doi.org/10.1016/j.surfcoat.2024.130761.
[21] Md Ahasan, M.J. Davidson, N. Selvakumar, Experimental investigations on the densification and deformation behaviour of al-Tib2 composite preforms, Trans. Indian Inst. Met. 69 (2016) 1059–1068, https://doi.org/10.1007/s12666-015-0622-9.
[22] Md Ahasan, M.J. Davidson, Modeling aspects of hot densification and deformation studies on Al–TiB2 composite preforms, Mater. Manuf. Process. 30 (2015) 1190–1195, https://doi.org/10.1080/10426914.2015.1019099.
[23] Md Ahasan, D.S. Chandramouli, R. Prasad, N. Pradeep, Ch Shashikanth, A prediction model based on simulation (FEA) and response surface methodology (RSM) for sintered al–tib2 preforms, Trans. Indian Inst. Met. 77 (2024) 3499–3506, https://doi.org/10.1007/s12666-024-03364-2.
[24] X.K. Zeng, Y.T. Li, X.D. Zhang, M. Liu, J.Z. Ye, X.L. Qiu, et al., Effect of bias voltage on the structure and properties of cunitinbcr dual-phase high entropy alloy films, J. Alloys Compd. 931 (2023) 167371, https://doi.org/10.1016/j.jallcom.2022.167371.
[25] S. Xia, W. Yang, Z. Tong, Microstructure and nano-hardness of reduced activation fecrv-based high entropy alloys with abundant ti addition, J. Mater. Eng. Perform. (2024), https://doi.org/10.1007/s11665-024-09995-2.
[26] K. Yue, L. Wang, Z. Xu, C. Cheng, Y. Wang, Y. Fan, et al., Effect of ti addition on the microstructure and corrosion behavior of laser cladding alcocrfeni high-entropy alloy coatings, Vacuum 230 (2024) 113633, https://doi.org/10.1016/j.vacuum.2024.113633.
[27] W. Liu, P. Wang, C. Wang, Y. Liu, S. Zhao, X. Nai, et al., Obtaining in-situ reacted Fe–W–Ni–Cr–cu high-entropy alloy within the interlayer of dissimilar CF/SIC-GH3536 joint by designing non-high-entropy Cu–ti–w composite filler, Mater. Sci. Eng., A 913 (2024) 147116, https://doi.org/10.1016/j.msea.2024.147116.
[28] Y. Meng, Z. Yang, Y. Shi, X. Liu, L. Wang, Q. Zhang, et al., Microstructural evolution and enhanced properties of multi-layer tizrnbcrco high entropy alloy coatings laser-clad onto ti–6al–4v alloy, Intermetallics 173 (2024) 108407, https://doi.org/10.1016/j.intermet.2024.108407.
[29] Y.J. Kwon, Y.J. Won, K.S. Cho, Thermodynamic evaluation of the phase stability in mechanically alloyed alcuxnicoti high-entropy alloys, J. Alloys Compd. 948 (2023) 169772, https://doi.org/10.1016/j.jallcom.2023.169772.
[30] X. An, F. Li, L. Kan, W. Zhang, J. Wang, X. Jin, et al., Synergistic enhancement of 7075 aluminum alloy composites via high entropy alloy particle integration: microstructural and mechanical insights, Mater. Chem. Phys. 328 (2024) 129988, https://doi.org/10.1016/j.matchemphys.2024.129988.
[31] A. Basem, M.A. Hassan, O.A. Elkady, Y.A. El-Shekeil, S. Bendoukha, N. Barhoumi, et al., Characterization of feconicr high-entropy alloys manufactured by Powder metallurgy technique, J. Mater. Res. Technol. 30 (2024) 88–100, https://doi.org/10.1016/j.jmrt.2024.03.054.
[32] M. Feng, T. Lin, G. Lian, C. Chen, X. Huang, Effects of Nb content on the microstructure and properties of cocrfemnninbx high-entropy alloy coatings by laser cladding, J. Mater. Res. Technol. 28 (2024) 3835–3848, https://doi.org/10.1016/j.jmrt.2024.01.002.
[33] M. Navazani, S.R. Kada, D. Fabijanic, M. Barnett, Increasing ductility via cu addition in alxcrfemnni: towards a scrap-based high entropy alloy, Intermetallics 164 (2024) 108100, https://doi.org/10.1016/j.intermet.2023.108100.
[34] Y. Garip, Tailoring oxidation resistance of FE2COCRNI0.5 based high entropy alloys by addition of alloying elements (si, Cu and Si-Cu co-added), J. Alloys Compd. 920 (2022) 165951, https://doi.org/10.1016/j.jallcom.2022.165951.